

Terahertz Probing of Anisotropic Conductivity and Morphology of CuMnAs Epitaxial Thin Films

Peter Kubaščík,* Andrej Farkaš, Kamil Olejník, Tinkara Troha, Matěj Hývl, Filip Krizek, Deep Chandra Joshi, Tomáš Ostatnický, Jiří Jechumtál, Miloš Surýnek, Eva Schmoranzarová, Richard P. Champion, Jakub Zázvorka, Vít Novák, Petr Kužel, Tomáš Jungwirth, Petr Němec, and Lukáš Nádvorník

Antiferromagnetic CuMnAs thin films have attracted attention since the discovery of the manipulation of their magnetic structure via electrical, optical, and terahertz pulses, enabling convenient approaches for switching between magnetoresistive states of the film for information storage. However, the magnetic structure and, thus, the efficiency of the manipulation can be affected by the film morphology and growth defects. In this study, the properties of CuMnAs thin films are investigated by probing the asymmetrical growth-related uniaxial anisotropy of electric conductivity by contact-free terahertz transmission spectroscopy. It is shown that the terahertz measurements conveniently detect the conductivity anisotropy that is consistent with conventional DC Hall-bar measurements. Moreover, the terahertz technique allows for considerably finer determination of anisotropy axes, and it is less sensitive to the local film degradation. Thanks to the averaging over a large detection area, the THz probing also allows an analysis of strongly non-uniform thin films. Using scanning electron and near-field terahertz microscopies, the observed anisotropic conductivity of CuMnAs is related to the elongation and orientation of growth defects, which both originate in the anisotropic growth of the films. In addition, control over the morphology of defects is demonstrated by using vicinal substrates.

technology thanks to their advantages as compared to ferromagnets: the insensitivity to external magnetic fields up to units or tens of Tesla improving the memory robustness,^[1,2] no stray fields, and the associated possibility of a denser memory bit integration,^[3] significantly faster coherent dynamics of the magnetic order reaching or exceeding the THz frequency scale,^[4] and availability of a large variety of AF materials ranging from insulators to metals.^[5,6]

However, the lack of a net magnetic moment of AFs also brings a significant challenge for the concept of a room-temperature device operation as impractically strong magnetic fields would be needed to manipulate the AF order. In this regard, the room-temperature collinear AF CuMnAs has gained significant attention thanks to the theoretical prediction^[7] and recent demonstrations of a coherent switching of the Néel vector by electrical current pulses.^[8–11] Besides its coherent reorientation, the magnetic order of CuMnAs can also be

1. Introduction

Antiferromagnets (AFs) have appeared on the roadmap towards future spintronic applications in information and memory

manipulated incoherently through heat-activated processes induced by electrical,^[12] optical,^[2] and THz pulses,^[13,14] resulting in a metastable nano-fragmentation of AF domains,^[2,15,16] called

P. Kubaščík, A. Farkaš, D. C. Joshi, T. Ostatnický, J. Jechumtál, M. Surýnek, E. Schmoranzarová, J. Zázvorka, P. Němec, L. Nádvorník
 Faculty of Mathematics and Physics
 Charles University
 Ke Karlovu 3, Prague 2 12116, Czech Republic
 E-mail: peter.kubascik@matfyz.cuni.cz

A. Farkaš, K. Olejník, M. Hývl, F. Krizek, V. Novák, T. Jungwirth
 Institute of Physics of the Czech Academy of Sciences
 Cukrovarnická 10, Prague 6 16200, Czech Republic
 T. Troha, P. Kužel
 Institute of Physics of the Czech Academy of Sciences
 Na Slovance 2, Prague 8 18200, Czech Republic
 R. P. Champion, T. Jungwirth
 School of Physics and Astronomy
 University of Nottingham
 Nottingham NG7 2RD, UK

The ORCID identification number(s) for the author(s) of this article can be found under <https://doi.org/10.1002/apxr.202300075>

© 2023 The Authors. Advanced Physics Research published by Wiley-VCH GmbH. This is an open access article under the terms of the Creative Commons Attribution License, which permits use, distribution and reproduction in any medium, provided the original work is properly cited.

DOI: 10.1002/apxr.202300075

Quench-switching. The nano-fragmentation is accompanied by a switching of the resistive state by tens of percent and has been explored in the context of logic-in-memory devices for spiking neuromorphic applications.^[2,12]

Consistently with previous studies,^[11–14] we prepare the tetragonal CuMnAs films (space group P4/nmm) by molecular beam epitaxy (MBE) on GaP, GaAs, and Si substrates.^[17,18] A detailed characterization^[19] of MBE-grown CuMnAs showed that the crystal growth is accompanied by a formation of several types of defects associated with externally controlled parameters, such as stoichiometry, choice of substrate, and layer thickness d . For example, polar GaP and GaAs substrates promote a growth mode that starts from the formation of isolated elongated islands. Upon increasing the deposition time, the islands gradually evolve into a percolated layer containing an array of elongated holes whose density decreases with increasing d . In contrast, the shape of islands formed during the growth on the non-polar Si substrate remains isotropic for all d .

All the types of defects contribute to film inhomogeneities and induce local variations of conductivity. In addition, the elongated defects also create local morphologic anisotropy which has been observed together with a global anisotropy of conductivity of CuMnAs thin films.^[14,19] Moreover, it could also contribute to the magnetic anisotropy^[20] and thus, be linked to the efficiency of the switching of the magnetic order. Therefore, a convenient detection method, a detailed understanding, and even a manipulation of the morphologic anisotropy are desirable for improving the overall performance of CuMnAs-based devices and could bring new functionalities.

In this paper, we show that a reliable contactless non-destructive detection of the anisotropy of electrical conductivity and related elongation of growth defects of CuMnAs is possible by means of the time-domain THz spectroscopy. This method probes the electrical properties averaged over a large film area defined by the THz spot size ($\approx 1 \text{ mm}^2$). These are orders of magnitude larger dimensions than the typical defect size ($< 1 \mu\text{m}$). Benefiting from this low sensitivity to local layer inhomogeneities and the high azimuthal angle resolution of the method, we find a correlation between the conductivity anisotropy and the anisotropy of elongated defects. Based on the spectral dependence of THz conductivity, we conclude that the source of the conductivity anisotropy is a bulk-material property induced by the asymmetrical growth of films. In addition, we show that Si substrates with vicinal (step-like) surfaces can be used to control the morphologic and conductivity anisotropy. Finally, by employing a scanning near-field THz microscopy, we directly observe a local increase of the electrical conductivity in elongated defects, demonstrating a growth-related variation of the transport properties in CuMnAs.

2. Experimental Details

2.1. Samples and Setups

The sample set consists of single-crystalline thin films of CuMnAs with various thicknesses (9–50 nm) grown by MBE on the three different (001)-oriented substrates (in most cases double-side polished): Si, GaP, and GaAs, as summarized in Table S1 (Supporting Information). Since our aim is to study the defect

morphology associated with elongated islands formed in the initial stages of the growth, we intentionally select samples in which this initial island growth mode was well pronounced. The [100] crystal direction of the CuMnAs epilayer is oriented along the [110] direction of the substrate.^[19] In the following text and Figures, the marked crystallographic directions refer to the substrate. The CuMnAs films were capped by 3 nm of Al which almost entirely oxidized in the air and formed a protective aluminium oxide (AlOx) cap. The surface was then lithographically patterned according to the experimental scheme used to determine the film conductivity (see **Figure 1** and Section 6: Experimental Section for more details).

The main, contactless technique used in our work is the THz time-domain transmission spectroscopy^[21] (scheme shown in Figure 1a), which is an established method for probing ultrafast electrical currents^[22–25] and conductivity.^[26,27] Here, linearly polarized picosecond pulses of THz radiation, generated by an excitation of a spintronic emitter^[28,29] by a train of ultrashort optical pulses (see Section 6 for more details), are focused to a $\approx 860 \mu\text{m}$ wide spot (see Figure S1, Supporting Information). The radiation is further transmitted through the CuMnAs film and substrate, with the substrate crystallographic axis [110] rotated by an angle α with respect to the polarization direction of the THz pulse. The transmitted radiation $E(t)$ is detected by the electrooptical sampling resulting in a signal $S(t)$. Since its image in the frequency domain, $S(\omega)$, equals the product of the transmitted field $E(\omega)$ and the transfer function of the setup, we can relate the detected signals to the conductivity $\sigma(\omega)$ of the CuMnAs film by the Tinkham formula^[22,30,31]:

$$\sigma(\omega, \alpha) = \frac{n_s(\omega) + n_A}{Z_0 d} \left(\frac{1}{t'(\omega, \alpha)} - 1 \right) \quad (1)$$

where $n_s(\omega)$ and $n_A = 1$ are refractive indices of the substrate and air, respectively, $Z_0 \approx 377 \Omega$ is the vacuum impedance, d is the thickness of CuMnAs, and $t'(\omega, \alpha) = S(\omega, \alpha)/S_{\text{ref}}(\omega, \alpha)$. Here, S_{ref} is the electrooptical signal for transmission through the bare substrate (see Section 6; Note S1, Supporting Information, for more details). For switching between S and S_{ref} , a chessboard-like pattern was created by non-etched and etched squares of the film (Figure 1c and Section 6 for details) to directly access the reference transmission through the substrate.

To get additional insight into the local variations of conductivity, a THz scanning near-field optical microscopy (THz-SNOM) setup^[32] was employed (see Figure 1b and Section 6). Although the scattered THz electric field depends on complicated near-field interactions between the sample and the SNOM tip, it can provide a qualitative relation between the growth defects, their topology, and the local conductivity of the CuMnAs film.

As a reference, the DC conductivity is determined by conventional electrical 4-probe measurements on lithographically defined Hall bars (length 250 μm , width 50 μm) patterned along selected crystallographic directions (Figure 1d), including the [110] and [1-10] directions where the anisotropy of conductivity is the most pronounced. The Hall bars are distributed over an area comparable to the dimensions of the THz spot ($\approx 1 \text{ mm}^2$), however, each individual Hall bar probes only $\approx 1\%$ of this area. Measurements by all techniques are performed at room temperature.

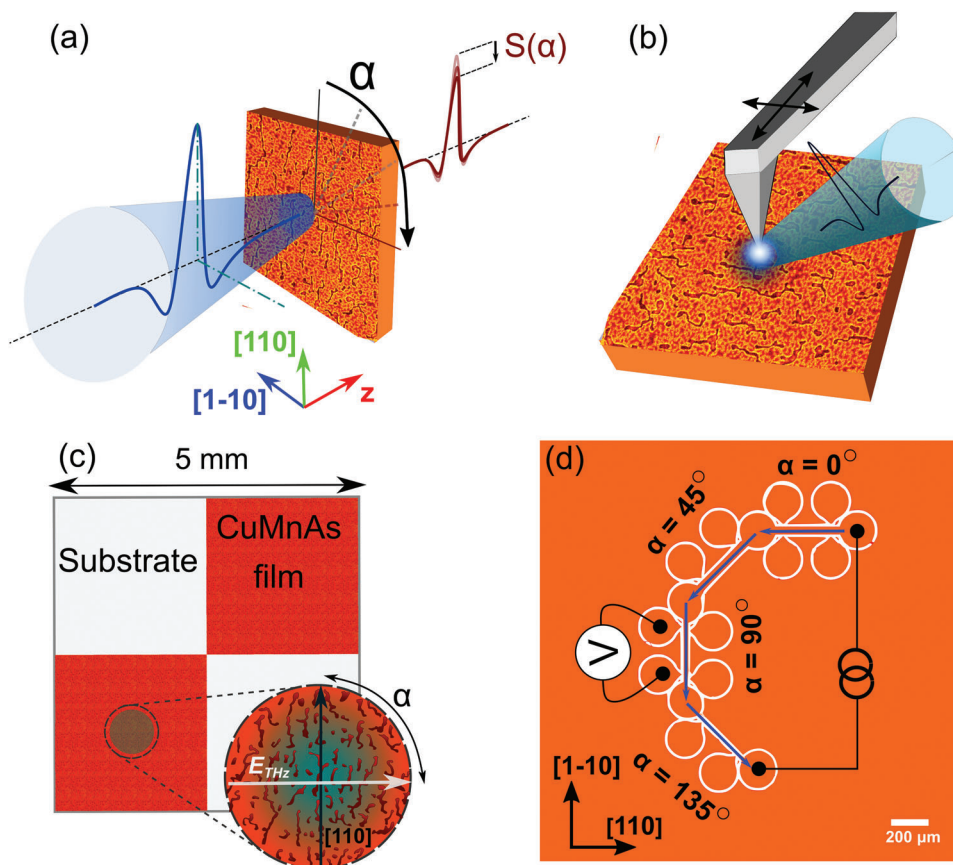


Figure 1. Samples and experimental schemes. a) A schematic of the THz transmission probing of the conductivity σ_{THz} of CuMnAs films. The incident linearly polarized THz pulse is transmitted through the film with [110] substrate crystal direction forming an angle α with the fixed polarization plane. The amplitude of the transmitted THz pulse is reduced due to σ_{THz} in the polarization direction. The anisotropy of $\sigma_{\text{THz}}(\alpha)$ is then inferred from the electrooptical signal $S(\alpha)$ of the transmitted pulse. b) A sketch of the THz sSNOM setup where the THz pulse is focused on the sample surface and a scanning tip, resulting in a near-field interaction with a resolution of ≈ 50 nm. The scattered THz radiation is related to the local σ_{THz} . c) The chessboard pattern of CuMnAs films (orange areas) used for THz experiments. The drawing depicts the advantage of the contactless method: accessing the global characteristics by averaging local responses with an arbitrary angular resolution of α without an impact of inhomogeneity of the film. d) A sketch of the lithographically prepared Hall bar device for DC electrical characterization. The electrical current (≈ 100 μA) is sent through Hall bar segments (blue arrows) oriented under four angles $\alpha = 0^\circ, 45^\circ, 90^\circ,$ and 135° with respect to [110] substrate crystal direction; the measured drop of potential provides the local resistance $R(\alpha)$.

3. Results

3.1. Raw THz Signals

Figure 2a shows typical THz transmission waveforms $S(t)$ through a 20 nm thick CuMnAs film on a GaP substrate, and the corresponding spectra, covering the frequency range of 0.3–2.2 THz (inset in Figure 2a). When we rotate the polarization direction from [110] axis of the substrate, i.e., increase α from 0 to 90°, the amplitude of $S(t)$ is clearly reduced. Consistently, the spectra are reduced in amplitude and no other spectral changes are observed. Since the overall shape of the THz trace is not changed, we can explore the α -dependence of the signal amplitude by taking the root-mean-square (RMS) of each waveform $S(t)$, normalizing its offset (average over α) to unity and plotting it in Figure 2b. The observed twofold symmetry of the RMS amplitude $S_N(\alpha)$ is emphasized by fitting the data by $\Delta \text{Scos}[2(\alpha + \alpha_0)] + 1$; the fit yields a modulation of $2\Delta S = 16.6\%$ and $\alpha_0 = 1.5^\circ$.

To show that the amplitude variation originates uniquely in the CuMnAs layer, we compare the data to RMS of the transmission signals through the bare substrate (Figure 2b, green data, α -average rescaled to unity), which shows a maximal variation of 0.6% (rest of samples are shown in Figure S2, Supporting Information). In addition, the symmetry of the signal is different, approaching a onefold (unidirectional) pattern. Another verification of the origin of the modulation is provided by conventional DC electrical characterization of the thin film. The hexagonal symbols in Figure 2b, right axis, represent the resistance R_{DC} measured in segments of the Hall bar oriented under an angle α . The twofold modulation and the phase of the signals agree well with the THz data, and the value of R_{DC} along the [110] direction is consistent with electrical measurements, reported previously on similar layers.^[19]

From the above qualitative findings, we conclude that the observed modulation of the THz signal originates in the thin film and is directly related to the anisotropic conductivity of CuMnAs.

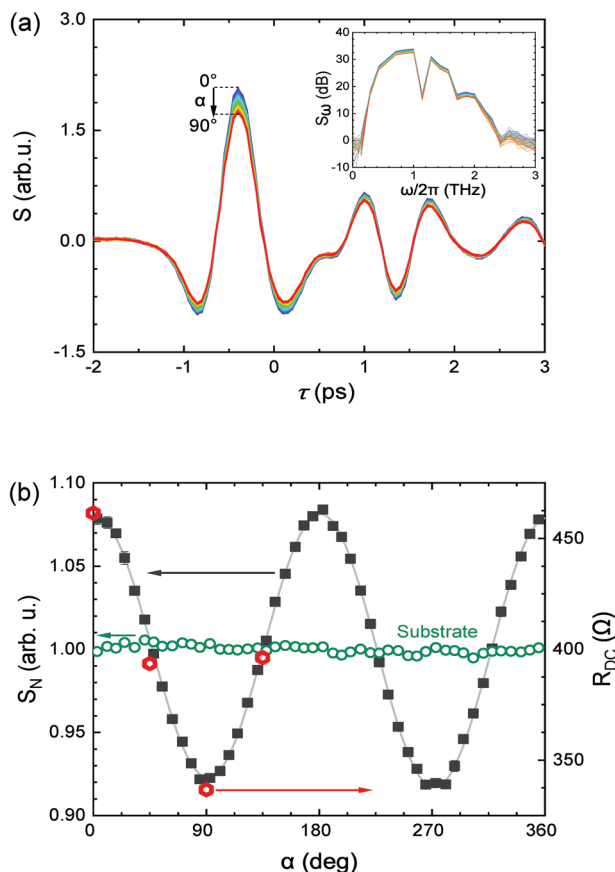


Figure 2. THz transmission signals. a) Typical THz transmission traces $S(t)$ for various rotation angles $\alpha = 0 - 90^\circ$ in 20 nm thick CuMnAs on GaP. Inset: Corresponding spectra S_ω . b) Left axis: extracted RMS amplitudes $S_N(\alpha)$ of traces transmitted through the sample (full black squares) and bare substrate (green open circles) as a function of α . Average of S_N over α is normalized to unity for both data sets. The fit (gray curve) is $\Delta S \cos[2(\alpha + \alpha_0)] + 1$, yielding $2\Delta S = 16.6\%$ and $\alpha_0 = 1.5^\circ$. Right axis: DC electrical resistance R_{DC} (red hexagonal points) measured using the Hall bar device.

Moreover, the modulation has a phase consistent with the orientation of previously reported elongated surface defects (their elongated direction was observed to be parallel to the [110] crystallographic direction of the substrate).^[19]

3.2. THz and DC Conductivities

To address the quantitative comparison of both methods, we first extract the complex-valued conductivity, $\sigma_{THz}(\omega)$, from the THz data for $\alpha = 0^\circ, 45^\circ$, and 90° using Equation (1) and correct it for possible phase shifts due to a variation of the substrate thickness (see also Note S1, Supporting Information). We fit the data by the Drude model^[31] which was shown to be well usable for CuMnAs thin films in our previous work^[14]:

$$\sigma_{THz}(\omega) = \frac{\sigma_{THz,0}}{1 - i\omega\tau} \quad (2)$$

where $\sigma_{THz,0}$ is the conductivity at $\omega = 0$, and τ is the electron scattering time (the mean time of the electron momentum randomization). The data and the fits are shown in Figure 3. Apart

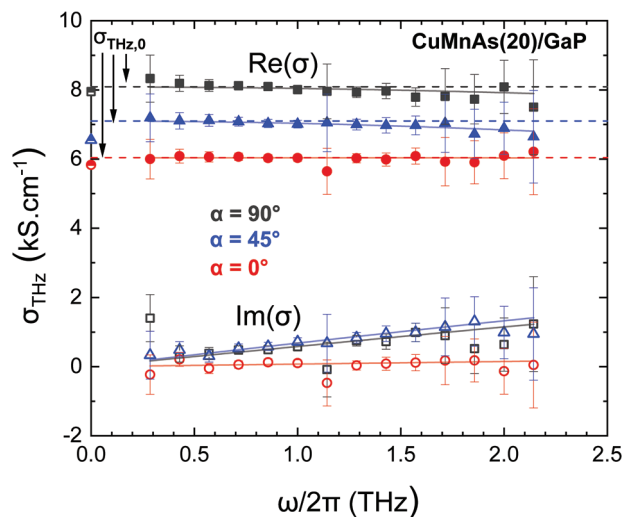


Figure 3. THz conductivity. Extracted real (full symbols) and imaginary parts (open symbols) of THz conductivity $\sigma_{THz}(\omega)$ for 20 nm thick CuMnAs on GaP using Equation (1) for three different orientations α of the sample. The solid curves are fit by the Drude model (Equation (2)). The value of the fit parameter $\sigma_{0,THz}$ is obtained from Equation (2) and plotted by dashed horizontal lines. The data points at $\omega = 0$ are the DC conductivities σ_{DC} .

from a significant variation of $\sigma_{THz,0}$ versus α by $\approx 30\%$ due to the anisotropy, we observe that the real part of σ_{THz} remains nearly constant over the studied frequency range. This implies that (i) we can view the film as fully percolated with no significant portion of insulated islands of CuMnAs. In non-percolated films, $\sigma_{THz}(\omega)$ typically differs from the Drude behavior and would be manifested by an increase of $\text{Re}(\sigma_{THz})$ with increasing frequency^[27,33] (a comparison to the Drude-Smith model is commented in Note 1, Supporting Information). Also, (ii) the real part of $\sigma_{THz}(\omega)$ can be approximated by constant $\sigma_{THz,0}$. The conclusions hold also for other samples (see Figure S3, Supporting Information). We can directly compare $\sigma_{THz,0}$ to the DC conductivity $\sigma_{DC} = l/(sdR_{DC})$ where l and s are the length and width of Hall bar segments between the voltage contacts (data points at $\omega = 0$ in Figure 3).

The conclusion (ii) allows us to avoid extraction of the spectral dependence of the conductivity and to simplify the subsequent systematic anisotropy study by disregarding the time dependence of $S(t)$ and only evaluating its RMS, $\text{rms}[S(t)]$. The quantity $\sigma_{THz,0}$ is then obtained by using Equation (1) and substituting $t' = \text{rms}[S(t)]/\text{rms}[S_{ref}(t)]$. The full dependence of $\sigma_{THz,0}$ and σ_{DC} on α , is plotted in Figure 4a by full red and open red data points, respectively. We observe a good quantitative agreement between the two methods, yielding the same conductivity anisotropy $2\Delta\sigma/\bar{\sigma} = 29.3\%$, where $2\Delta\sigma$ is the full amplitude of modulation of conductivity and $\bar{\sigma}$ is α -averaged mean conductivity.

An example of the analysis of samples on other substrates is shown in Figure 4 ($S_N(\alpha)$ and $\sigma_{THz,0}(\alpha)$ for the whole sample set are available in Figures S2 and S4, Supporting Information, respectively). In contrast to GaP and GaAs substrates (Figure 4a,b), we observe a significant discrepancy between $\sigma_{THz,0}$ (full blue points) and σ_{DC} (open pink points) for CuMnAs films grown on

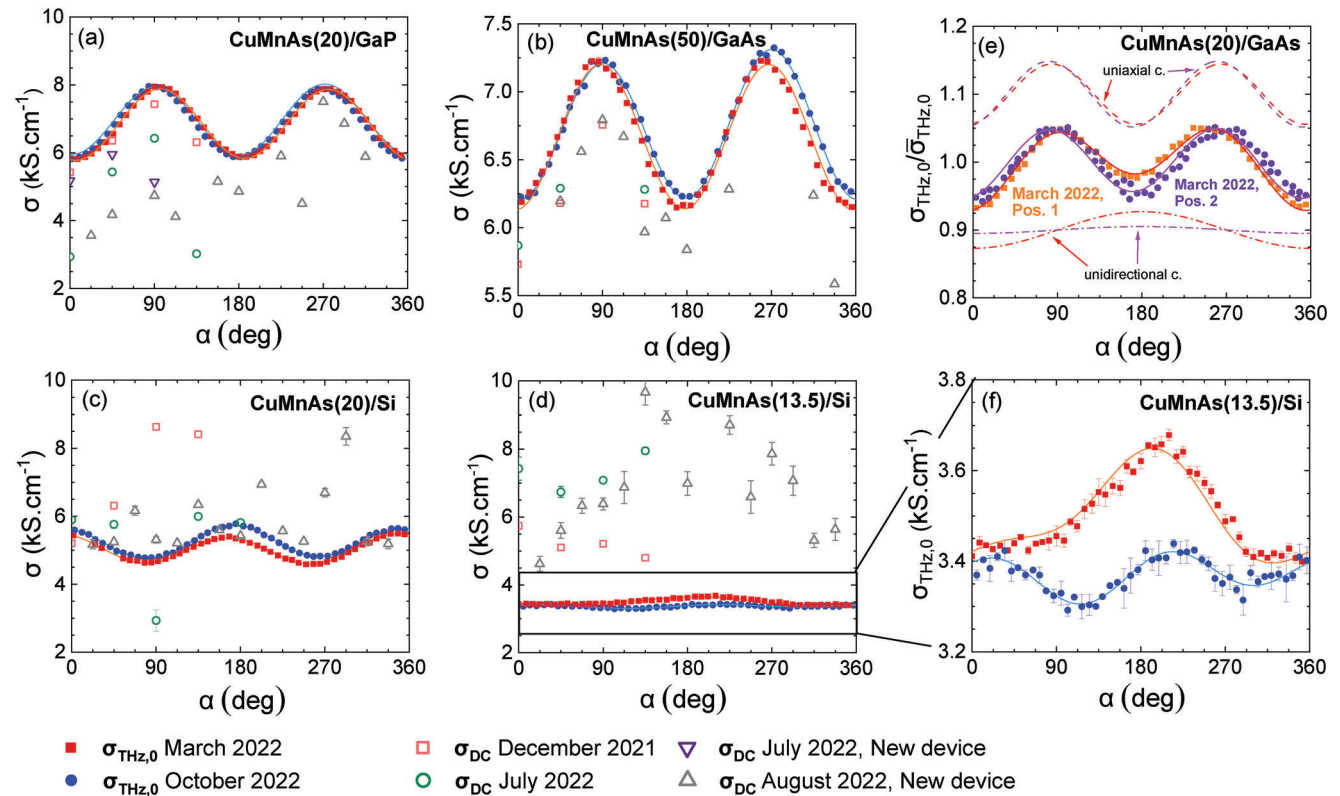


Figure 4. THz versus DC anisotropy of conductivity. $\sigma(\alpha, \omega)$ obtained from the THz data ($\sigma_{\text{THz},0}$; full symbols) and DC measurements (σ_{DC} ; open symbols) for various CuMnAs samples. a) 20 nm thick CuMnAs on GaP substrate, b) 50 nm on GaAs, c) 20 nm on Si, and d) 13.5 nm on Si, measured at various times (see time labels below the plots). Solid curves are fit by Equation (3). e) $\sigma_{\text{THz},0}$ measured in March 2022 with 20 nm thick CuMnAs on GaAs substrate in two different areas, separated by ≈ 1 mm (in the horizontal [1-10] substrate direction for $\alpha = 0$). Dashed curves are the twofold (uniaxial) contributions of the fit by Equation (3), and the onefold (unidirectional) contributions are shown in dash-and-dot curves. These components are shifted vertically for clarity. f) A close-up on $\sigma_{\text{THz},0}$ data of (d).

the Si substrate (Figure 4c,d). To address the possible impact of inhomogeneity and gradual oxidation of the films on both methods, we repeated the experiments after 7–8 months on the same samples: at a different location on the surface (THz data, full red points), at the same location using the original Hall bar devices (DC data, open green points) and on a new location using newly patterned devices (DC data, open purple points). Finally, we performed DC measurements on new devices with Hallbars rotated by 22.5° (open gray points). We observe that, apart from CuMnAs(50)/GaAs, all DC measurements differ significantly from each other. Even their scatter increased over the time period, while the THz data are significantly more consistent. These findings indicate that the DC electrical detection of the σ anisotropy is more prone to the degradation of CuMnAs due to local oxidation, an effect which was reported even on capped films.^[19] The oxidation affects the edges and holes in the film and the degradation is even accelerated at the uncapped vertical edges of etched-out structures. This leads to possible damage to the devices and deterioration of their functionality. The THz detection is not impacted by the local oxidation to this extent as it averages over the area of the sample probed by the THz spot which is significantly larger than the local degradation areas. For this reason, only the THz data will be analyzed in the rest of this section.

Although noticeably more reproducible, the THz data still show a certain deviation from the expected $\cos(2\alpha)$ dependence with indications of different symmetry with respect to α . Therefore, we evaluate the relative contribution of the uniaxial (twofold, $\Delta\sigma_2$) and unidirectional (onefold, $\Delta\sigma_1$) components by fitting the THz data by an empirical function

$$\sigma_{\text{THz},0}(\alpha) = \Delta\sigma_1 \cos(\alpha + \alpha_1) + \Delta\sigma_2 \cos[2(\alpha + \alpha_2)] + \bar{\sigma} \quad (3)$$

where α_1 and α_2 are the corresponding phases of modulations, i.e., orientations of the anisotropic axes for unidirectional and uniaxial components, respectively. Results of the fits of all the studied samples are summarized in Table S1 (Supporting Information) and later in Figure 5. While $\Delta\sigma_2 \gg \Delta\sigma_1$ and phase $\alpha_2 \approx 90^\circ$ stays constant for all films on GaP and GaAs substrates, this does not hold for the Si substrate: the phase reverses its sign in Figure 4c, and the weaker anisotropy of $\sigma_{\text{THz},0}$ can even be dominated by $\Delta\sigma_1$, as seen in Figure 4d and its close-up Figure 4f. Here, we see that $\Delta\sigma_1$ changed dramatically with changing the probing position and the measurement time period. To get more insight into the nature of $\Delta\sigma_1$, we repeated the experiment with CuMnAs(20)/GaAs on the same day and in two different sample locations separated by roughly 1 mm in the [1-10] direction

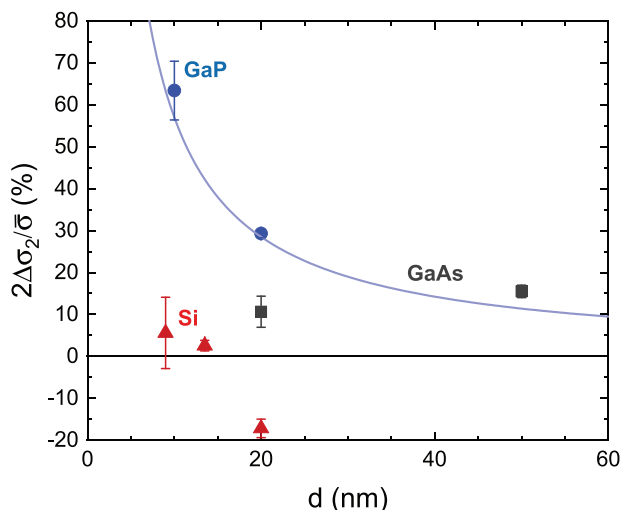


Figure 5. Thickness dependence of conductivity anisotropy. The twofold component $2\Delta\sigma_2/\bar{\sigma}$ of the conductivity modulation as a function of the film thickness d for three substrates (circles: GaP, squares: GaAs, triangles: Si) obtained from fits of THz data (March 2022) in Figure 4. Error bars are the magnitude of the onefold component $\pm 2\Delta\sigma_1/\bar{\sigma}$. In correspondence with Ref. [19], a $1/d$ -dependence is plotted as a guide for an eye for GaP (solid blue curve). The opposite phase of $\sigma_{0,\text{THz}}(\alpha)$ for CuMnAs(20)/Si is emphasized by plotting it as a negative number.

(Figure 4e). While $\Delta\sigma_2$ stays the same for both locations, the $\Delta\sigma_1$ component significantly changes. A consistent observation is made for the corresponding phases: α_1 varies randomly for all measured samples (illustrated in Figure S5, Supporting Information). From these observations, we draw a conclusion that the unidirectional (onefold) symmetry is an artifact. A slight misalignment of the sample rotation axis and the propagation axis of the THz pulses can lead to an effective motion of the THz spot over the surface. Indeed, the characterization of the maximal possible displacement of the THz spot on the sample surface during the sample rotation yielded $\approx 40 \mu\text{m}$ (Note 2 and Figure S6, Supporting Information). This, in combination with large-scale gradients of the film and the substrate, can lead to an apparent non-zero $\Delta\sigma_1$. Therefore, the genuine anisotropy of the electrical conductivity seems to be only the uniaxial component.

The elongated-defect-related uniaxial anisotropy component of the conductivity, $2\Delta\sigma_2/\bar{\sigma}$, for different d and substrates is shown in Figure 5, complemented by a guide to the eye (blue curve) to highlight the expected trends for the samples on the GaP substrate.^[19] Conservatively, the error bars are set as the magnitude of the corresponding unidirectional anisotropy component $\Delta\sigma_1/\bar{\sigma}$. We observe that $2\Delta\sigma_2/\bar{\sigma}$ measured on CuMnAs/GaP decreases with the film thickness, while the sample on GaAs yields an unexpected increasing trend. Similarly, relatively small values of $2\Delta\sigma_2/\bar{\sigma}$, approaching zero within the error bars, on the two CuMnAs/Si samples for $d < 14$ nm are contrasted by a 20 nm thick CuMnAs/Si sample with $2\Delta\sigma_2/\bar{\sigma} = 17.2\%$ and an opposite phase to the films on GaP and GaAs. To stress this phase change, the value of $2\Delta\sigma_2/\bar{\sigma}$ is plotted with a negative sign in Figure 5. We note that all samples were remeasured on multiple surface regions, consistently yielding the presented results. To understand these trends, we further explored the film defects morphology.

3.3. Surface Defect Morphology

The morphology of surface defects can be observed directly by performing scanning electron microscopy (SEM) imaging of the sample surfaces and inferring the corresponding defect aspect ratio AR . We illustrate the analysis on two samples with significant differences in their conductivity anisotropy: 10-nm-thick CuMnAs/GaP ($2\Delta\sigma_2/\bar{\sigma} = 63.4\%$) and 9-nm-thick CuMnAs/Si ($2\Delta\sigma_2/\bar{\sigma} < 3\%$), whose SEM images are shown in Figure 6a,b, respectively. The SEM images for all samples are shown in Figure S7 (Supporting Information). We note that a part of the SEM image of CuMnAs(20)/GaP was removed from the analysis in order to suppress surface contamination. Overall, a clear elongation of defects is observed along the [110] GaP substrate direction (indicating $AR > 1$), while rather isotropic surface defects are evidenced in the film on Si substrate ($AR \approx 1$).

To quantify AR of the defects, we numerically processed the SEM images by the edge-finding method, described in Section 6, yielding histograms of defect dimensions, w , in [110] and [1-10] directions (Figure 6c,d). By evaluation of average values of defect dimension in [110] and [1-10], we inferred $AR = \mu_{[110]}/\mu_{[1-10]}$ where μ_i is the expected values (average) of the distribution in the respective direction i . The analysis yields $AR \approx 1.6$ and ≈ 1 for the CuMnAs(10)/GaP and the CuMnAs(9)/Si sample, respectively. The results of this analysis for all samples are summarized in Figure 6e, where their $2\Delta\sigma_2/\bar{\sigma}$ are plotted as a function of the corresponding defect AR . The observed trend directly reveals a correlation between these two quantities (shown in Figure 6e by a guide to the eye). Remarkably, the scaling between the conductivity anisotropy and AR holds also for the measurements on GaAs and Si substrates where we found unexpected trends of the conductivity anisotropy versus thickness d (Figure 5). The increased $2\Delta\sigma_2/\bar{\sigma}$ in thicker CuMnAs/GaAs is, indeed, related to more elongated defects in this sample, and the surprisingly large conductivity anisotropy in CuMnAs(20)/Si also scales well with the determined AR . Moreover, the reversed phase α_2 of $\sigma_{\text{THz},0}(\alpha)$ in this sample is consistent with the elongation of defects in the [1-10] substrate direction (opposite to CuMnAs on GaP and GaAs), yielding $AR < 1$. This motivates us to verify whether such a small AR of CuMnAs films on non-polar Si substrates can be related to the substrate parameters.

3.4. Effect of Vicinal Substrates

Inducing the anisotropic properties of thin films by growth on vicinal substrates is a known technique used in MBE deposition.^[34] For example, a significant anisotropy in the conductivity of isotropic metals,^[35] semiconducting quantum wells,^[36] or in the morphology of microstructural defects in semiconducting thin films^[37] has been observed on miscut (100) Si substrates. To address whether an unintentional miscut of the used substrates could explain the negative and large AR of the CuMnAs(20)/Si film, the atomic force microscopy (AFM) imaging of the etched-off substrate part of the sample was performed in Figure 6f. Here, we can indeed observe small terraces-like features in the form of asymmetric “saw-like” modulation of the surface (more details in Figure S8, Supporting Information), indicating a possible small vicinality in the order of 0.1° .

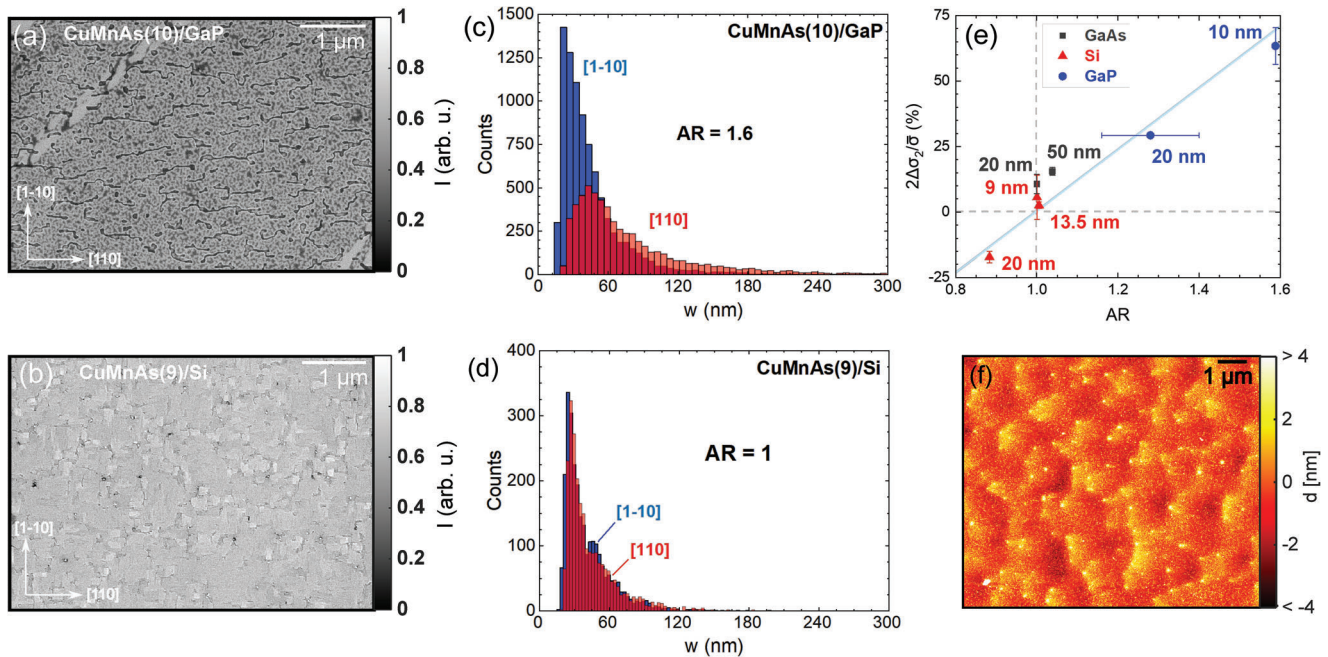


Figure 6. Correlation of THz conductivity modulation with defect morphology. SEM images of a) CuMnAs(10)/GaP and b) CuMnAs(9)/Si films with c, d) corresponding histograms of defect size (w) distributions in [110] and [1-10] substrate directions. e) Twofold component of the conductivity modulation $2\Delta\sigma_2/\bar{\sigma}$ as a function of the defect aspect ratio. The blue line is a guide for the eye. Error bars are considered as $\pm 2\Delta\sigma_1/\bar{\sigma}$. f) An AFM image of the etched-off substrate part of CuMnAs(20)/Si sample, showing terrace-like surface structures.

To further test the hypothesis, the sample set was complemented by three 20 nm thick CuMnAs films grown in a series under identical conditions on two intentionally miscut GaAs substrates of the vicinity of 2° in [110] or [1-10] directions and on a reference non-vicinal GaAs substrate. The obtained conductivity modulation $\sigma_{\text{THz},0}(\alpha)$ is plotted in **Figure 7a**. The sample grown on the reference non-vicinal GaAs substrate shows consistently a similar modulation, $2\Delta\sigma_2/\bar{\sigma} = 9.1\%$ with $\alpha_2 = 95^\circ$, as compared to the CuMnAs(20)/GaAs sample shown in **Figure 5** and grown in a different MBE chamber. In contrast, the sample on the [1-10]-vicinal substrate shows a considerably higher anisotropy ($2\Delta\sigma_2/\bar{\sigma} = 16.1\%$, $\alpha_2 = 93^\circ$), caused by a formation of defects elongated in the [110] direction. Interestingly, the [110]-miscut substrate even leads to an anisotropy in the perpendicular direction ($2\Delta\sigma_2/\bar{\sigma} = 7.1\%$, $\alpha_2 = 4^\circ$), surpassing the original anisotropy related to the polarity of the non-vicinal GaAs. From these findings, we conclude that the vicinity of substrates can affect the nucleation of defects during growth and it can even be used to control the resulting conductivity anisotropy.

3.5. Local Conductivity and Morphology

Finally, we complete the THz-spot-averaged conductivity measurements by a demonstration of probing of local THz conductivity σ_{loc} inside and outside a defect. The σ_{loc} of the CuMnAs(10)/GaP film was investigated by THz-SNOM (sketched in **Figure 1b**), yielding both the AFM-like maps of the surface, shown in **Figure 7b** as color maps, and the amplitude of the scattered THz pulses, presented as contours with labels indicating the relative THz amplitude decrease in percent. We observe a

clear correlation between the defects of the film and the locally scattered THz amplitude. If we limit ourselves only to a qualitative observation, we can interpret the findings as a clear correspondence between the surface morphology and σ_{loc} and, in particular, as an increase of σ_{loc} inside the defect, i.e., in the region where the local film thickness is reduced. This could indicate a change of bulk transport properties inside defects.

4. Discussion

The presented experiments show that the time-domain THz spectroscopy is a reliable, fast, and versatile method to quantify the anisotropic conductivity of CuMnAs and, potentially, of other thin films. The extracted angular modulation of the conductivity is consistent over multiple repeated measurements and with conventional DC electrical characterization. Compared to the DC probing using Hall bars, it brings several advantages: i) It is non-destructive and contactless as it requires no surface patterning. ii) It provides a high angular resolution of practically arbitrary precision of α , which is limited in the case of DC characterization by the number of patterned devices, allowing for a precise determination of anisotropic axes and exclusion of parasitic contributions of other than uniaxial (twofold) symmetries in the signal. iii) Since the THz probing of the conductivity is averaged over an arbitrarily large area according to a chosen spot size (in our case $\approx 1 \text{ mm}^2$), a single experiment can yield statistically averaged conductivity and its anisotropy even in strongly non-uniform samples. The technique also allows for mapping of the gradual degradation of films, e.g. due to global surface oxidation, by monitoring the change of the area-averaged conductivity with a sensitivity given by the signal-to-noise ratio of the measurement (in our case

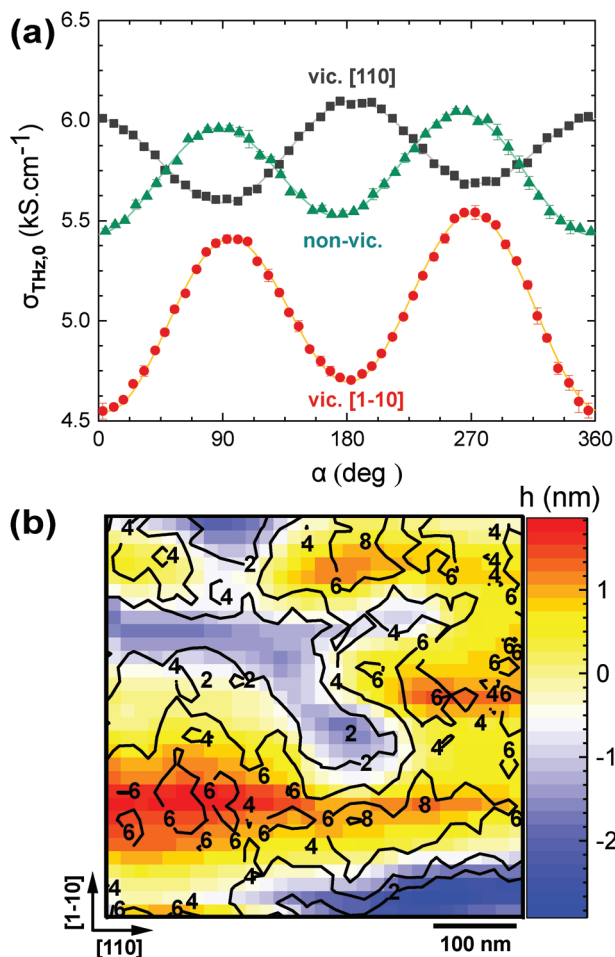


Figure 7. Manipulation of conductivity anisotropy by vicinal substrates and THz-SNOM measurements. a) Anisotropy of $\sigma_{\text{THz},0}$ in CuMnAs(20)/GaAs samples grown on normal (green points) and vicinal substrates with vicinality of 2° in direction [110] (black points) and [1-10] (red points). Curves with the corresponding colors are fitted by Equation 3. b) The relative amplitude decrease in the percent of the scattered THz pulses from CuMnAs(10)/GaP measured by the THz-SNOM scanning of the sample surface (contours with labels). The corresponding AFM image of the same area is shown by the color map.

the order-of-magnitude accuracy of the conductivity is $\approx 0.1\%$ for 45 s long measurement). For applications where a more local characterization is needed, for example, homogeneity checks for device micro-fabrication, the technique should be complemented by THz-sSNOM measurements or electrical probing.

The THz conductivity $\sigma_{\text{THz}}(\omega)$ of CuMnAs films were well described by the Drude model for all crystal orientations and its value extrapolated to zero frequency was consistent with the DC characterization (Figure 3). This implies that the THz short-range transport parameters are the same as the global ones probed by the Hall-bar technique and that the short-range boundary scattering is not dominantly impacting the transport.^[27,38–40] Interestingly, the Drude-like $\sigma_{\text{THz}}(\omega)$ and a good consistency of DC and extrapolated THz values are not restricted only to CuMnAs or other single-crystalline films,^[41] but they are also often observed in thin films of polycrystalline non-magnetic^[29,42] and magnetic

metals,^[30,31] including their multilayers.^[43] Although the presented method can be a good characterization tool in single- and polycrystalline films where the grain boundaries cause only a small perturbation in the drift mobility of free carriers, the extrapolation of $\sigma_{\text{THz}}(\omega)$ to DC should be done with caution.

The flat spectral dependence of $\sigma_{\text{THz}}(\omega)$, excluding a significant role of the short-range scattering at boundaries of growth defects, strongly indicates that the observed anisotropy of $\sigma_{\text{THz}}(\omega)$ arises from a bulk property of the material. This anisotropic bulk property is likely to be induced during the anisotropic MBE growth due to the reported different speeds of atomic diffusion on the polar III-V surfaces^[19] or vicinal substrates.^[35] Since the origin of the elongated defects is explained by the same physical process,^[19] the transport anisotropy of the bulk is expected to be strongly correlated with the aspect ratio AR of defects. Our experimental findings directly confirm this picture as the size of the anisotropic conductivity, $2\Delta\sigma_2/\bar{\sigma}$, showed a linear dependence on AR for all the studied CuMnAs films (Figure 6e).

The global anisotropy of $\sigma_{\text{THz}}(\omega)$ and σ_{DC} can originate from the anisotropic bulk properties: i) only inside defects or ii) of the whole film. The explanation that locates the source (i) inside a defect is supported by the THz-SNOM measurements, reporting a higher local conductivity σ_{loc} of the material inside the defect than outside of them. We note that the increase of σ_{loc} cannot be explained simply by a variation in local film thickness which decreases inside defects (Figure 7b). This shows that the transport properties can be locally affected during and due to the anisotropic growth, but our data cannot provide information about their anisotropy. For such investigation, the experimentally challenging polarization-resolved THz near-field microscopy experiment could be conducted inside a defect.^[44–46] On the other hand, if the transport anisotropy is (ii) the bulk property of the entire layer, the defects serve here as indicators of the orientation and strength of this anisotropy since both arise from the same origin – the anisotropic growth. Vice versa, thanks to this link between the defects and the conductivity anisotropy, $\sigma_{\text{THz}}(\alpha)$ can be used for a fast and non-destructive determination of the orientation and AR of the growth-induced defects. Indeed, our measurement revealed an unexpected defect anisotropy of CuMnAs on non-polar Si substrate, indicating an unintentional miscut in the used Si wafer.

The possibility to control the induced defect AR and related anisotropic conductivity using intentionally vicinal substrates can play an important role in the magnetic recording in CuMnAs. The shape and orientation of defects with a size on the order of tens of nanometers, i.e., the same range as observed in our samples (Figure 6c), were shown to affect the magnetic anisotropy in AF. They lead to an effective shape-induced magnetic anisotropy,^[20] even though AF possesses vanishingly small net magnetization. Indeed, very recently, Reimers *et al.* directly experimentally showed by photoemission electron microscopy and X-ray diffraction techniques that the magnetic domain structure in CuMnAs thin films is correlated with their growth defects.^[47]

5. Conclusion

In summary, we have shown that THz time-domain spectroscopy can be used to measure the asymmetrical growth-related

anisotropic conductivity and related growth defects of CuMnAs thin films in a reliable, contactless, and versatile manner. The method also proved to be less sensitive to the film degradation as compared to the electrical characterization by Hall bars, requiring lithographic processing. At the same time, it allows for an analysis of strongly non-uniform thin films due to the averaging of the conductivity over the large area of the THz spot size. The uniaxial conductivity anisotropy was observed on samples with various thicknesses and grown on GaP, GaAs, and Si substrates. Its magnitude and orientation with respect to the crystallographic directions in the sample were correlated with the elongation and orientation of growth defects and its origin was identified as an anisotropic transport property of the bulk induced by the anisotropic growth. We also demonstrated that the anisotropic conductivity can be controlled not only by the film thickness but also by using vicinal Si substrates. The understanding and control of defect morphology, presented in this paper, can lead to future optimization of spintronic functionality in AF devices based on CuMnAs.

6. Experimental Section

Hall Bar Fabrication: For the fabrication of the chessboard-like structure (Figure 1c) and the Hall-bar devices (Figure 1d), first, a positive photoresist was deposited on the sample by spin-coating and baked on the hotplate. Next, the resist was exposed maskless photolithography machine, developed using an alkaline developer, and etched in a 1:400 solution of phosphoric acid.

Electrical Measurements: Electrical measurements were carried out with two electrical setups, one consisting of Keithley SourceMeter 2400 (current source) and Keithley MultiMeter 2000 (voltmeter) and the other utilizing NI DAQ card USB-6211. In the first setup, the readout current was set to 100 μ A to prevent heating, and, in the case of the second setup, the reading voltage was set to 0.2 V, and the readout current was measured as a voltage drop over a known resistor. Corresponding voltages were measured with a four-point method for each segment in the Hall bar. The conductivity in the corresponding direction was calculated from the known dimensions of segments.

THz Measurements: Time Domain THz Spectroscopy: The linearly polarized picosecond pulses of THz radiation were generated by exciting the spintronic emitter^[29,48] by a train of laser pulses (1030 nm, 170 fs long, fluence 0.15 mJcm⁻², repetition rate 10 kHz) and focused on the sample, forming a \approx 800 μ m wide spot (FWHM). The transmitted radiation $E(t)$ was detected by the electrooptical sampling using a 110-cut 2 mm thick GaP crystal,^[21] yielding the electrical signal $S(t)$. Since its image in the frequency domain, $S(\omega)$, equals the product of the transfer function of the setup and the transmitted field $E(\omega)$, the transfer function cancels^[24,49] in ratio $S(\omega, \alpha)/S_{\text{ref}}(\omega, \alpha) = E(\omega, \alpha)/E_{\text{ref}}(\omega, \alpha) = t'$ where S_{ref} and E_{ref} are the electrooptical signal and electric field for transmission through the bare substrate.

To study the anisotropy of transmission, the sample was attached to a rotational holder with an angular resolution of 0.2°. If the THz beam axis and the axis of rotation of the holder do not coincide, small displacements of the beam spot on the sample surface are induced during the sample rotation. To avoid this, a special alignment technique was introduced (see Note 2, Supporting Information). After the alignment, samples were installed with a precision of \approx 2° into the rotational holder without moving it. The measured angular dependence of THz transmission was globally shifted by 3° due to the THz polarization rotation tilt from the vertical direction induced by parabolical mirrors (see Figure S9, Supporting Information).

THz-sSNOM: A THz scanning near-field optical microscope THz-SNOM (Neaspec) was used to investigate local changes in conductivity. Broadband THz pulses (0.2–1.5 THz) are focused on a PtIr tip (50 nm

radius) that oscillates above the film surface with the typical tapping frequency of 50–100 kHz (Figure 1b). The detected scattered THz electric field carries information about the local conductivity. Scanning the sample surface with the tip thus provides local conductivity measurements with a spatial resolution of \approx 50 nm. The simplest models used to describe the underlying physics consider the electrostatic approach. In this case, the near-field contribution to the scattered THz electric field can be expressed as $E_{\text{scatt}} \propto (1 + r_p)^2 \alpha_{\text{eff}} E_{\text{inc}}$, where E_{inc} is the incident field, α_{eff} is the effective tip polarizability, and r_p the Fresnel reflection coefficient for p -polarized light.^[50,51] The near-field interaction between the sample and the tip (and consequently the local conductivity) is incorporated in α_{eff} which depends nonlinearly on the tip-sample distance. As a result of the tip oscillation α_{eff} is modulated at the tip frequency as well as at higher harmonics of the tip frequency. By demodulating the THz signal at higher demodulation orders, the useful signal, which depends on the local conductivity, could be extracted efficiently. A 2D scan of the sample surface (Figure 7b) was obtained by scanning the sample surface at the peak electric field of the scattered THz pulse detected at the second demodulation order. The quantitative determination of the local conductivity requires an appropriate model for the description of the whole system. However, on a qualitative level, THz signals could be related to variations of local conductivity.

Microscopic Imaging: Scanning Electron Microscopy: The SEM analysis is based on quantifying the dimensions of growth defects along the two orthogonal directions (in x - and y -axis). For each pixel row/column of recorded images, cuts were applied along the x and y directions, analysed by a peak finder method and the identified peaks fitted by Gaussian functions. The defect size w is then inferred as the $1/e$ -half-width of the Gaussian. From the obtained distributions of w in [110] and [1-10] directions, the average values $\mu_{[110]}$ and $\mu_{[1-10]}$, respectively, were evaluated and the corresponding aspect ratio $AR = \mu_{[110]}/\mu_{[1-10]}$ was estimated (more details in Note 3, Supporting Information).

Atomic Force Microscopy: For all AFM scans, Bruker Dimension ICON AFM was operated in semi-contact Peak Force QNM mode using Aspire conical force modulation (CFM) probes. The symmetrical shape and combination of small tip radius (guaranteed < 10 nm) and sharp tip cone angle (30°) of these probes ensure true and symmetrical representation of all sample features. For processing the data, Gwyddion software^[52] was used with a focus on local surface roughness, disregarding the natural slope of the sample surface.

Supporting Information

Supporting Information is available from the Wiley Online Library or from the author.

Acknowledgements

The authors would like to thank Jan Zubáč for fruitful discussions. The authors acknowledge funding by the Czech Science Foundation through projects GA CR (Grant No. 2128876) and 1928375X), the Grant Agency of the Charles University (grants No. 166123 and SVV-2023260720), the Operational Program Research, Development, and Education financed by the European Structural and Investment Funds and the Czech Ministry of Education, Youth and Sports (Project No. SOLID21 CZ.02.1.01/0.0/0.0/16/019/0000760). The authors also acknowledge CzechNanoLab Research Infrastructure supported by MEYS CR (LM2023051). J.Z. acknowledges the support of Charles University grant PRIMUS/20/SCI/018.

Conflict of Interest

The authors declare no conflict of interest.

Data Availability Statement

The data that support the findings of this study are available from the corresponding author upon reasonable request.

Keywords

antiferromagnetic spintronics, CuMnAs, growth defects, terahertz spectroscopy, vicinal substrates

Received: June 29, 2023

Revised: August 23, 2023

Published online: October 11, 2023

- [1] O. Gomonay, V. Baltz, A. Brataas, Y. Tserkovnyak, *Nanotechnology* **2018**, 29, 1.
- [2] Z. Kašpar, M. Surýnek, J. Zubáč, F. Krizek, V. Novák, R. P. Champion, M. S. Wörnle, P. Gambardella, X. Marti, P. Němec, K. W. Edmonds, S. Reimers, O. J. Amin, F. Maccherozzi, S. S. Dhesi, P. Wadley, J. Wunderlich, K. Olejník, T. Jungwirth *Nat. Electron.* **2021**, 4, 30.
- [3] M. B. Jungfleisch, W. Zhang, A. Hoffmann, *Phys. Lett. A* **2018**, 382, 865.
- [4] S. M. Rezende, A. Azevedo, R. L. Rodríguez-Suárez, *J. Appl. Phys.* **2019**, 126, 151101.
- [5] T. Jungwirth, X. Marti, P. Wadley, J. Wunderlich, *Nat. Nanotechnol.* **2016**, 11, 231.
- [6] V. Baltz, A. Manchon, M. Tsoi, T. Moriyama, T. Ono, Y. Tserkovnyak *Rev. Mod. Phys.* **2018**, 90, 15005.
- [7] J. Železný, H. Gao, K. Výborný, J. Zemen, J. Mašek, A. Manchon, J. Wunderlich, J. Sinova, T. Jungwirth *Phys. Rev. Lett.* **2014**, 113, 157201.
- [8] P. Wadley, B. Howells, J. Železný, C. Andrews, V. Hills, R. P. Champion, V. Novák, K. Olejník, F. Maccherozzi, S. S. Dhesi, S. Y. Martin, T. Wagner, J. Wunderlich, F. Freimuth, Y. Mokrousov, J. Kuneš, J. S. Chauhan, M. J. Grzybowski, A. W. Rushforth, K. W. Edmonds, B. L. Gallagher, T. Jungwirth, *Science* **2016**, 351, 587.
- [9] P. Wadley, S. Reimers, M. J. Grzybowski, C. Andrews, M. Wang, J. S. Chauhan, B. L. Gallagher, R. P. Champion, K. W. Edmonds, S. S. Dhesi, F. Maccherozzi, V. Novák, J. Wunderlich, T. Jungwirth *Nat. Nanotechnol.* **2018**, 13, 362.
- [10] J. Godinho, H. Reichlová, D. Kriegner, V. Novák, K. Olejník, Z. Kašpar, Z. Šobáň, P. Wadley, R. P. Champion, R. M. Otxoa, P. E. Roy, J. Železný, T. Jungwirth, J. Wunderlich *Nat. Commun.* **2018**, 9, 4686.
- [11] K. A. Omari, L. X. Barton, O. Amin, R. P. Champion, A. W. Rushforth, A. J. Kent, P. Wadley, K. W. Edmonds *J. Appl. Phys.* **2020**, 127, 193906.
- [12] K. Olejník, V. Schuler, X. Marti, V. Novák, Z. Kašpar, P. Wadley, R. P. Champion, K. W. Edmonds, B. L. Gallagher, J. Garcés, M. Baumgartner, P. Gambardella, T. Jungwirth *Nat. Commun.* **2017**, 8, 15434.
- [13] K. Olejník, T. S. Seifert, Z. Kašpar, V. Novák, P. Wadley, R. P. Champion, M. Baumgartner, P. Gambardella, P. Němec, J. Wunderlich, J. Sinova, P. Kužel, M. Müller, T. Kampfrath, T. Jungwirth *Sci. Adv.* **2018**, 4, eaar3566.
- [14] J. J. F. Heitz, L. Nádvořník, V. Balos, Y. Behovits, A. L. Chekhov, T. S. Seifert, K. Olejník, Z. Kašpar, K. Geishendorf, V. Novák, R. P. Champion, M. Wolf, T. Jungwirth, T. Kampfrath *Phys. Rev. Appl.* **2021**, 16, 64047.
- [15] F. Krizek, S. Reimers, Z. Kašpar, A. Marmodoro, J. Michalička, O. Man, A. Edström, O. J. Amin, K. W. Edmonds, R. P. Champion, F. Maccherozzi, S. S. Dhesi, J. Zubáč, D. Kriegner, D. Carbone, J. Železný, K. Výborný, K. Olejník, V. Novák, J. Ruzs, J.-C. Idrobo, P. Wadley, T. Jungwirth *Sci. Adv.* **2022**, 8, eabn3535.
- [16] M. Surýnek, V. Saidl, Z. Kašpar, V. Novák, R. P. Champion, P. Wadley, P. Němec *J. Appl. Phys.* **2020**, 127, 233904.
- [17] P. Wadley, V. Novák, R. P. Champion, C. Rinaldi, X. Martí, H. Reichlová, J. Železný, J. Gazquez, M. A. Roldan, M. Varela, D. Khalyavin, S. Langridge, D. Kriegner, F. Máca, J. Mašek, R. Bertacco, V. Holý, A. W. Rushforth, K. W. Edmonds, B. L. Gallagher, C. T. Foxon, J. Wunderlich, T. Jungwirth *Nat. Commun.* **2013**, 4, 2322.
- [18] P. Wadley, V. Hills, M. R. Shahedkhan, K. W. Edmonds, R. P. Champion, V. Novák, B. Ouladdiaf, D. Khalyavin, S. Langridge, V. Saidl, P. Nemeč, A. W. Rushforth, B. L. Gallagher, S. S. Dhesi, F. Maccherozzi, J. Železný, T. Jungwirth *Sci. Rep.* **2015**, 5, 17079.
- [19] F. Krizek, Z. Kašpar, A. Vetushka, D. Kriegner, E. M. Fiordaliso, J. Michalíčka, O. Man, J. Zubáč, M. Brajer, V. A. Hills, K. W. Edmonds, P. Wadley, R. P. Champion, K. Olejník, T. Jungwirth, V. Novák *Phys. Rev. Mater.* **2020**, 4, 14409.
- [20] O. Gomonay, S. Kondovych, V. Loktev, *J. Magn. Magn. Mater.* **2014**, 354, 125.
- [21] Y.-S. Lee, in *Principles of Terahertz Science and Technology*, Vol. 170, Springer, NY, USA **2009**.
- [22] D. Yagodin, L. Nádvořník, O. Gueckstock, C. Gahl, T. Kampfrath, K. I. Bolotin, *2D Mater.* **2021**, 8, 25012.
- [23] E. T. Papaioannou, R. Beigang, *Nanophotonics* **2020**, 10, 1243.
- [24] P. Jiménez-Cavero, O. Gueckstock, L. Nádvořník, I. Lucas, T. S. Seifert, M. Wolf, R. Rouzegar, P. W. Brouwer, S. Becker, G. Jakob, M. Kläui, C. Guo, C. Wan, X. Han, Z. Jin, H. Zhao, D. Wu, L. Morellón, T. Kampfrath *Phys. Rev. B* **2022**, 105, 184408.
- [25] R. Rouzegar, L. Brandt, L. Nádvořník, D. A. Reiss, A. L. Chekhov, O. Gueckstock, C. In, M. Wolf, T. S. Seifert, P. W. Brouwer, G. Woltersdorf, T. Kampfrath *Phys. Rev. B* **2022**, 106, 144427.
- [26] J. Lloyd-Hughes, T.-I. Jeon, *J. Infrared, Millimeter, Terahertz Waves* **2012**, 33, 871.
- [27] P. Kužel, H. Němec, *Adv. Opt. Mater.* **2020**, 8, 1900623.
- [28] T. S. Seifert, S. Jaiswal, U. Martens, J. Hannegan, L. Braun, P. Maldonado, F. Freimuth, A. Kronenberg, J. Henrizi, I. Radu, E. Beaupaire, Y. Mokrousov, P. M. Oppeneer, M. Jourdan, G. Jakob, D. Turchinovich, L. M. Hayden, M. Wolf, M. Münzenberg, M. Kläui, T. Kampfrath *Nat. Photonics* **2016**, 10, 483.
- [29] T. S. Seifert, L. Cheng, Z. Wei, T. Kampfrath, J. Qi, *Appl. Phys. Lett.* **2022**, 120, 180401.
- [30] T. S. Seifert, U. Martens, F. Radu, M. Ribow, M. Berritta, L. Nádvořník, R. Starke, T. Jungwirth, M. Wolf, I. Radu, M. Münzenberg, P. M. Oppeneer, G. Woltersdorf, T. Kampfrath *Adv. Mater.* **2021**, 33, 2007398.
- [31] L. Nádvořník, M. Borchert, L. Brandt, R. Schlitz, K. A. de Mare, K. Výborný, I. Mertig, G. Jakob, M. Kläui, S. T. B. Goennenwein, M. Wolf, G. Woltersdorf, T. Kampfrath, *Phys. Rev. X* **2021**, 11, 21030.
- [32] M. M. Wiecha, A. Soltani, H. G. Roskos, in *Terahertz Technology*, In-techOpen, London, UK **2021**.
- [33] P. Kužel, H. Němec, *J. Phys. D: Appl. Phys.* **2014**, 47, 374005.
- [34] K. Seshan, in *Handbook of Thin Film Deposition Techniques Principles, Methods, Equipment and Applications*, 2nd ed., CRC Press, FL, USA **2002**.
- [35] T. López-Ríos, A. Briggs, S. Guillet, A. M. Baro, M. Luna, *Appl. Phys. Lett.* **1995**, 66, 529.
- [36] P. Waltereit, J. M. Fernández, S. Kaya, T. J. Thornton, *Appl. Phys. Lett.* **1998**, 72, 2262.
- [37] M. Calamiotou, N. Chrysanthakopoulos, Ch. Lioutas, K. Tsagaraki, A. Georgakilas, *J. Cryst. Growth* **2001**, 227-228, 98.
- [38] N. Laman, D. Grischkowsky, *Appl. Phys. Lett.* **2008**, 93, 051105
- [39] K. Shimakawa, F. Kadlec, K. Kadlec, J. Prikryl, T. Wagner, M. Frumar, S. Kasap *Phys. status solidi (RRL)–Rapid Res. Lett.* **2021**, 15, 2000411.
- [40] J. C. Delagnes, P. Mounaix, H. Němec, L. Fekete, F. Kadlec, P. Kužel, M. Martin, J. Mangeney *J. Phys. D: Appl. Phys.* **2009**, 42, 195103.
- [41] K. L. Krewer, W. Zhang, J. Arabski, G. Schmerber, E. Beaupaire, M. Bonn, D. Turchinovich *Appl. Phys. Lett.* **2020**, 116, 102406.

- [42] M. Meinert, D. Graulich, T. Matalla-Wagner, *Phys. Rev. Appl.* **2018**, *9*, 64040.
- [43] Z. Jin, A. Tkach, F. Casper, V. Spetter, H. Grimm, A. Thomas, T. Kampfrath, M. Bonn, M. Kläui, D. Turchinovich *Nat. Phys.* **2015**, *11*, 761.
- [44] T. L. Cocker, V. Jelic, R. Hillenbrand, F. A. Hegmann, *Nat. Photonics* **2021**, *15*, 558.
- [45] B. Gompf, N. Gebert, H. Heer, M. Dressel, *Appl. Phys. Lett.* **2007**, *90*, 082104.
- [46] S. Schäffer, A. K. Wigger, P. H. Bolívar, presented at *2018 43rd Intl. Conf. on Infrared, Millimeter, and Terahertz Waves*, IEEE, Nagoya, Japan **2018**.
- [47] S. Reimers, D. Kriegner, O. Gomonay, D. Carbone, F. Krizek, V. Novák, R. P. Champion, F. Maccherozzi, A. Björling, O. J. Amin, L. X. Barton, S. F. Poole, K. A. Omari, J. Michalička, O. Man, J. Sinova, T. Jungwirth, P. Wadley, S. S. Dhesi, K. W. Edmonds *Nat. Commun.* **2022**, *13*, 724.
- [48] O. Gueckstock, L. Nádvorník, T. S. Seifert, M. Borchert, G. Jakob, G. Schmidt, G. Woltersdorf, M. Kläui, M. Wolf, T. Kampfrath *Optica* **2021**, *8*, 1013.
- [49] O. Gueckstock, R. L. Seeger, T. S. Seifert, S. Auffret, S. Gambarelli, J. N. Kirchof, K. I. Bolotin, V. Baltz, T. Kampfrath, L. Nádvorník *Appl. Phys. Lett.* **2022**, *120*, 62408.
- [50] A. Cvitkovic, N. Ocelic, R. Hillenbrand, *Opt. Express* **2007**, *15*, 8550.
- [51] M. M. Wiecha, R. Kapoor, H. G. Roskos, *APL Photonics* **2021**, *6*, 126108.
- [52] D. Nečas, P. Klapetek, *Cent. Eur. J. Phys.* **2012**, *10*, 181.